

The Decrease of Specific Angular Momentum and the Hot Toroid Formation: The Massive Clump G10.6-0.4

Hauyu Baobab Liu^{1,2,3}

Harvard-Smithsonian Center for Astrophysics, 60 Garden Street, Cambridge, MA 02138

`hlu@cfa.harvard.edu`

Paul T. P. Ho^{1,3}

*Academia Sinica Institute of Astronomy and Astrophysics,
P.O. Box 23-141, Taipei, Taiwan*

`pho@asiaa.sinica.edu.tw`

Qizhou Zhang¹

Eric Keto¹

Harvard-Smithsonian Center for Astrophysics, 60 Garden Street, Cambridge, MA 02138

`qzhang@cfa.harvard.edu`

`keto@cfa.harvard.edu`

Jingwen Wu⁵

Jet Propulsion Laboratory, 4800 Oak Grove Dr., Pasadena, CA, 91101

`Jingwen.Wu@jpl.nasa.gov`

Huabai Li⁴

Max Planck Institute for Astronomy, Königstuhl 17, D-69117 Heidelberg, Germany

`li@mpia.de`

¹Harvard-Smithsonian Center for Astrophysics

²Department of Physics, National Taiwan University

³Academia Sinica Institute of Astronomy and Astrophysics

⁴Max Planck Institute for Astronomy

⁵Jet Propulsion Laboratory

ABSTRACT

This is the first paper of our series of high resolution ($1''$) studies of the massive star forming region G10.6–0.4. We present the emission line observations of the hot core type tracers (O^{13}CS , OCS , SO_2) with $\sim 0''.5$ resolution. By comparing the results to the high-resolution NH_3 absorption line observation, we confirm for the first time the rotationally flattened hot toroid in the central <0.1 pc region, which has a rotational axis perpendicular to its geometrical major axis.

In addition, we present the observations of NH_3 , ^{13}CS , and CH_3CN with $\sim 1''$ resolution, and follow the dynamics of the molecular accretion flow from the 0.3 pc radius to the inner 0.03 pc radius. With reference to the rotational axis of the hot toroid, we measure the rotational velocity from the molecular emission in the region. The results are consistent with an envelope with a rapid decrease of the specific angular momentum from the outer to the inner region. These new results improve the current understanding of the molecular accretion flow in an ultracompact (UC) HII region created by the embedded O-type cluster.

Subject headings: stars: formation — ISM: evolution — ISM: individual (G10.6–0.4)

1. Introduction

Rotational motions are commonly observed in massive star forming regions (see Cesaroni et al. 2007 for a general review). Growing observational evidence shows that rotating flattened core or disk-like structure (10^1 – 10^2 M_\odot , 1000–8000 AU) and massive molecular outflows (Zhang et al. 2001, 2005; Beuther et al. 2002) are commonly present in B-type star forming regions, suggesting that disks are closely related to the collapse of the molecular core. The estimated mass infall rates in these disks range from 10^{-3} $M_\odot\text{yr}^{-1}$ to 10^{-5} $M_\odot\text{yr}^{-1}$, which are comparable to or much higher than the necessary mass accretion rates to form B-type stars (Zhang 2005 and references therein). The well-studied examples of the O-type star forming regions, however, are limited, and the properties of their rotational structures are less clear. Rotational signatures have been reported toward several sources such as G24.78+0.08, G28.20–0.05, G31.41+0.31, G10.6–0.4, G16.59–0.05, G23.01–0.41, G28.87+0.07 and G20.08–0.14n (Beltrán et al. 2004, 2005; Sollins et al. 2005a, 2005b; Keto, Ho and Haschick 1987, 1988; Sollins and Ho 2005; Furuya et al. 2008; Klaassen et al. 2009; Galvan-Madrid et al. 2009). Owing to the complicated environments and their large distances, the properties of these rotating structures around the O-type star forming regions are not well investigated. In our present series of experiments, we start with the source G10.6–0.4 and establish a large molecular database with high sensitivity and high resolution ($<1''$, 0.03 pc). These lines

probe the physical conditions in *zones* with different excitation conditions. Our goals are to unveil the morphologies and to resolve the kinematical structures of these massive toroids.

The ultracompact (UC) HII region G10.6–0.4 is one of the best studied OB cluster forming regions. The associated infrared source IRAS 18075–1956 has a luminosity of $9.2 \times 10^5 L_{\odot}$ (Casoli et al. 1986). From the observations of the 20 cm continuum emissions, Ho, Klein, and Haschick (1986) detected the presence of OB stars in a ~ 10 pc region, and suggested that a burst of massive star formation occupies the central parsec region. The follow-up high resolution 6 cm and 1.3 cm continuum observations further suggest a concentration of OB stars in the central ~ 0.1 pc region, which ionizes a bright (> 2.6 Jy in 1.3 cm) UC HII region (Ho and Haschick 1986; Keto, Ho, and Haschick 1987, 1988; Sollins et al. 2005a; Sollins and Ho 2005). The detections of bright H_2O and OH masers (Ho et al. 1983; Hofner and Churchwell 1996; Fish et al. 2005; Lekht et al. 2006) around the peak of the centimeter continuum also suggest that this is an active site of massive star formation.

The early low resolution ($> 5''$) observations detect molecular lines in emission (NH_3 : Ho and Haschick 1986; Keto, Ho, and Haschick 1987; CS: Omodaka et al. 1992; $C^{18}O$: Ho, Terebey, and Turner 1994) and reveal a flattened rotating dense clump (G10-main hereafter) with a velocity gradient of $\sim 10 \text{ kms}^{-1} \text{ pc}^{-1}$ at a half parsec scale radius. High-resolution ($< 1''$) Very Large Array (VLA) observations on molecular lines have been carried out as well. However, limited by sensitivities, all previous high-resolution VLA observations (Keto, Ho and Haschick 1988; Guilloteau et al. 1988; Sollins et al. 2005; Sollins and Ho 2005) only see the absorption lines against the bright UC HII region, of which the detections are limited by the background illumination. For example, Keto, Ho, and Haschick (1988), Sollins et al. (2005a) and Sollins and Ho (2005) resolve the velocity gradient to be $\sim 90 \text{ kms}^{-1} \text{ pc}^{-1}$ in the central $2''$ (0.06 pc) region. Based on these observational results of the NH_3 (1,1), (3,3) inversion transitions and the radiative transfer simulations, Keto (1990) suggested that the gas dynamics in G10-main are consistent with a spin-up rotational motion. However, without the high resolution observations in emission lines, the geometry of the entire region is poorly constrained. The rotational axis is therefore uncertain, which potentially leads to the systematic bias in the derived velocity gradients. Also, how does the molecular gas flow continue from the parsec scale molecular clump to the central 0.1 pc scale region was not resolved yet.

In this paper, we report our high angular resolution and high sensitivity interferometric observations of various molecular transitions toward G10-main. These 1 mm observations are sensitive to high excitation lines which trace the gas close to the central stars. We constrain the location and the orientation of the rotational motions from our highest resolution ($< 1''$) observations of the hot core type tracers $O^{13}CS$, OCS, and SO_2 molecular transitions. The emissions of these transitions are only significantly detected in a $< 3''$ region around the UC HII region, and are therefore less confused by the dynamics of the complicated and more extended features. We call the rotating structure traced by the observed SO_2 , OCS, and $O^{13}CS$ emission the *hot toroid* hereafter. The size scale of the hot toroid is directly constrained by the detection of the selected hot core type tracers.

We then measure the velocity gradients traced by the stable molecules CH_3CN , ^{13}CS , C^{34}S , and NH_3 in the plane of the hot toroid. By utilizing the excitation conditions of these molecules, we constrain the rotational velocities from 0.6 pc to the central 0.1 pc scale. Combining with the previous lower resolution CS (1-0) (Omodaka et al. 1992) and NH_3 (1,1) inversion line (Ho and Haschick 1986; Keto, Ho, and Haschick 1987) observations which measure the velocity gradients over a more extended region, we track the loss of angular momentum continuously over a factor of ~ 50 in sizescale. In addition, we resolve the density concentration and the fragmentation signatures in the central 0.5 pc region. Details about the observations, and the data reductions are introduced in Section 2. The results and the method to analyze the rotational signature are presented in Section 3.

2. Observation and Data Reduction

We provide the detailed information of our observations, and the data reductions. The properties of the molecular line data are listed in Table 1. The observational parameters of the selected molecules are summarized in Table 2.

2.1. Line Observations

2.1.1. The CH_3CN Observations

We observed the CH_3CN J=12-11 transitions using the Submillimeter Array (SMA)¹ in the extended configuration on 2005 September 05. For more on the SMA and its specifications, see Ho, Moran & Lo (2004). The frequency resolution in that observation is 390 kHz ($\sim 0.53 \text{ kms}^{-1}$). The basic calibrations of these data are done in Miriad, and additional self-calibration on the source are done in Miriad, and imaging is done in AIPS.

In this paper, we present the CH_3CN 12(5)-11(5), and 12(6)-11(6) mapping results to trace the high temperature ($>250 \text{ K}$) and high density gas, observed to be concentrated to a small region close to the UC HII region (for more analysis of these CH_3CN data see Klaassen et al. 2009). Continuum emissions are averaged from the line-free channels and then subtracted from the line data. To enhance the signal-to-noise ratio, we average the visibilities of these two lines to form a synthesized line (CH_3CN K₅₆ line hereafter; these two transitions have upper energy levels of 242 K and 319 K, respectively). The signal to noise ratio will be enhanced by a factor of $\sqrt{2}$ if both the 12(5)-11(5) and the 12(6)-11(6) lines are detected. However, in regions where the temperature is not high enough to excite the 12(6)-11(6) transition, the signal to noise ratio will be degraded by

¹The Submillimeter Array is a joint project between the Smithsonian Astrophysical Observatory and the Academia Sinica Institute of Astronomy and Astrophysics, and is funded by the Smithsonian Institution and the Academia Sinica.

a factor of $\sqrt{2}$. Thus we argue that the temperature traced by the K_{56} line is biased to be higher than 300 K. We find that the emission of the K_{56} line is mainly contributed by the gas distributed within a 0.1 pc region of the UC HII region.

The CH_3CN line is imaged using natural weighting, which leads to the synthesized beam of $1''.5 \times 1''.1$ with position angle 56° . The observed rms noise for the channel maps is $0.12 \text{ Jy beam}^{-1}$.

2.1.2. The $^{13}\text{CS}/\text{C}^{34}\text{S}$ (5–4), $\text{OCS}/\text{O}^{13}\text{CS}$ (19–18) and SO_2 Observations

We observed the ^{13}CS (5–4), $\text{OCS}/\text{O}^{13}\text{CS}$ (19–18), SO_2 5(2,4)–4(1,3) and SO_2 18(1,17)–18(0,18) transitions toward G10.6–0.4 using the SMA in the compact configuration and the very extended configuration on 2009 June 10 and 2009 July 12, respectively. We also observed ^{13}CS (5–4) in the subcompact configuration on 2009 January 31. The frequency resolutions in these observations are 390 kHz ($\sim 0.53 \text{ kms}^{-1}$).

The basic calibrations are done in Miriad, while the self-calibration and imaging of these data are done in AIPS. Continuum emissions are averaged from the line-free channels and then subtracted from the line data. We combined the ^{13}CS data of all three array configurations, which yields a synthesized beam of $1''.3 \times 0''.66$ with a position angle 79° . The observed rms noise of the ^{13}CS (5–4) line channel maps is $0.05 \text{ Jy beam}^{-1}$. We combined the compact array and the very extended array data for the other molecules. To better constrain the geometry and velocity gradient in the 0.1 pc scale rotating core, we imaged the OCS and SO_2 lines using uniform weighting, yielding the highest angular resolution of $0''.62 \times 0''.43$ with a position angle 22° . We imaged the weaker O^{13}CS line using natural weighting to improve the signal-to-noise ratio. The C^{34}S line is imaged using *robust=0* for optimizing the resolution and sensitivity.

2.1.3. The NH_3 (3,3) Main Hyperfine Line Observations

We observed the NH_3 (3,3) main hyperfine line toward G10.6–0.4 ($\alpha(\text{J2000}) = 18^h 10^m 28^s.683$, $\delta(\text{J2000}) = -19^\circ 55' 49''.07$) using the NRAO² VLA in the C-configuration on 2009 July 27. The frequency resolution in these observations is 97.656 kHz ($\sim 1.23 \text{ kms}^{-1}$). We observed 3C286, 0319+415, and 1820–254 as our absolute flux, passband, and gain calibrators.

The basic calibrations, self-calibration, and imaging of these data are done in AIPS. The size of the synthesized beam is $1''.8 \times 1''.2$ with a position angle 0.96° , and the rms noise is 8 mJy beam^{-1} ($\sim 9 \text{ K}$). Continuum emissions are averaged from the line-free channels and then subtracted from the line data. Our data are consistent with the earlier NH_3 (3,3) D-array data reported in Keto,

²The National Radio Astronomy Observatory is a facility of the National Science Foundation operated under cooperative agreement by Associated Universities, Inc.

Ho, and Haschick (1987) when smoothed to the same resolution. However, our higher angular and velocity resolutions provide better constraints for the kinematics in the inner $10''$ (0.3 pc) region. For the NH_3 kinematics in the more extended (and cooler) region, we will directly quote the NH_3 (1,1) main hyperfine inversion transition result from Keto, Ho and Haschick (1987).

2.2. Continuum Observations

We construct the continuum band at 1.3 mm from the line-free channels in the SMA subcompact, compact, and very-extended array data mentioned in Section 2.1.2. We combined the data of all three array configurations, which yields the synthesized beam of $0''.79 \times 0''.58$ with position angle 60° . With the large 4 GHz total bandwidth, a low rms noise of 3 mJy beam^{-1} is achieved.

We also retrieved and reprocessed the 1.3 cm VLA A-array continuum data from the data archive. The synthesized beam of this 1.3 cm continuum map is $0''.12 \times 0''.07$ with position angle 58° . See Sollins et al. (2005) and Sollins and Ho (2005) for the detailed descriptions of these VLA continuum observations.

3. Results

3.1. The Continuum Emissions

Figure 1 shows the 1.3 mm and the 1.3 cm continuum emission maps. The comparison of the continuum emissions at these two frequencies suggests that

- Inwards of the $\sim 3''$ region, the 1.3 mm continuum is contributed by the free-free emission of the UC HII region and the thermal dust emissions.
- The 1.3 mm continuum is dominantly contributed by the thermal dust emission in the extended region.
- The extended dust emissions show clumpy and protrusive morphology.

The measured 1.3 mm continuum flux is about 10 Jy within a $10''$ (0.3 pc) region, and about 6 Jy within the central $4''$ region. By subtracting the measured 1.3 mm continuum flux with the predicted lower limit of free-free continuum flux at 1.3 mm (Keto, Zhang, and Kurtz 2008), we find that the upper limit of the thermal dust emission at 1.3 mm within the central $4''$ region is 2.7 Jy. Assuming an average temperature of 200 K and assuming a gas-to-dust mass ratio of 100, the 2.7 Jy flux corresponds to the H_2 mass of 140, 230 and 380 M_\odot for $\beta = 1, 1.5$ and 2, respectively (Lis et al. 1998). Assuming an average temperature of 50 K, without including the central $4''$ region, the H_2 mass estimated by dust emission is 240, 400, and 660 M_\odot for $\beta = 1, 1.5$ and 2, respectively. The

total H_2 mass enclosed in the central $10''$ region is therefore 240–1040 M_\odot . We note that extended emissions may have some missing flux, and the mass derivations for that region should be treated as the lower limit.

3.2. The OCS, O^{13}CS , SO_2 and CH_3CN Emissions —The Hot Toroid

Figure 2 shows the moment zero, one and two³ maps of the OCS (19–18) line, the O^{13}CS (19–18) line, the SO_2 18(1,17)–18(0,18) and 5(2,4)–4(1,3) lines, and the CH_3CN K_{56} line. From these maps, first we can see that these transitions are only detected in a small ($2''$ – $3''$) region around the UC HII region. From the moment 2 and moment 1 maps, we see that the local velocity dispersion is generally small as compared with the velocity range traced by each molecule, suggesting that the organized dynamics dominates over the thermal/turbulent motions. A prominent common dynamics feature detected by all these tracers is a velocity gradient from southeast to northwest along the major axis of the flattened structure, which suggests a rotating toroid. From the velocity gradient, we determined the position angle to be $140^\circ \pm 5^\circ$. The geometry of the CH_3CN emission appears to be more spherical, which is due to the relatively low resolution.

Assuming that the molecular abundance is uniform in the size scale of the hot toroid, the ratio of the O^{13}CS intensity to the OCS intensity shows the relative distribution of the column density. Figure 3 shows the ratio of the velocity integrated flux density of the O^{13}CS and the OCS lines⁴. From this figure we can see that the distribution of the dense molecular gas is consistent with a $\sim 2'' \times 1''$ toroid aligned along the southeast-northwest axis, and the $\text{O}^{13}\text{CS}/\text{OCS}$ ratio is about 0.2 in that region. By comparing the $\text{O}^{13}\text{CS}/\text{OCS}$ ratio maps with the high resolution NH_3 (3,3) satellite hyperfine line absorption optical depth maps (Figure 3, see Sollins et al. 2005a for the introduction of the high resolution NH_3 data), we can see that the dense molecular gases traced by these two molecules are in excellent agreement with each other, suggesting that these molecular line transitions are indeed tracing the hot and dense rotating toroid in the most central region. In this particular source, the UC HII region is optically thick in the centimeter band (Keto, Ho and Haschick 1987, 1988). We note that in the millimeter band, both the UC HII region and dust are optically thin, which allows us to probe the gas motions at the back or the far side of the UC HII region, and therefore improves the constraint on the gas kinematics as compared to previous centimeter band experiments (Keto, Ho and Haschick 1987, 1988; Sollins and Ho 2005). Assuming that the abundance ratio $[\text{OCS}]/[\text{O}^{13}\text{CS}]$ is 30 (Gibb et al. 2000), we obtain the average optical depth of the O^{13}CS and the OCS $\text{J}=19$ –18 transitions in the region with $>3\sigma$ detections to be 0.17 and 5.12, respectively. The detected brightness temperatures of the selected SO_2 lines are comparable to the brightness temperature of the OCS line. Therefore, we suggest that these lines

³The moment two is estimated from $\frac{\int v^2 F_v dv}{\int F_v dv}$.

⁴When generating this ratio map, both the OCS and the O^{13}CS (19–18) lines are imaged with natural weighting.

have a similar beam filling factor, and are generally optically thick.

It should be noted that our high resolution observations of these hot core and shock tracers suggest that the molecular gas in the central $3''$ (0.09 pc) region is fragmented and may be interacting with the ionized gas and the outflows. In this paper we focus on the discussion of the rotational signatures shown in these molecular line observations, which are specifically associated with the strong gravitational source, an OB cluster at the center. Discussions of the high velocity molecular outflows and shock signatures will be presented in a separate publication.

3.3. The Structure of Specific Angular Momentum

The molecules $^{13}\text{CS}/\text{C}^{34}\text{S}$, NH_3 and CH_3CN have relatively stable abundances as compared to the other hot core and shock tracers. The emission lines of these molecules trace a broad range of excitation conditions. By comparing the rotational signatures traced by these molecules, we successfully follow the rotational signature from a parsec scale radius to the central 0.03 pc radius around the OB cluster. We introduce the terminal velocity method to analyze the rotational velocity as a function of radius and show the decrease of specific angular momentum inward of the 0.3 pc radius.

3.3.1. The Spatial Distribution of Tracers

Figure 4 shows the moment zero map of the ^{13}CS (5-4) line, the NH_3 (3,3) main hyperfine inversion line, the CH_3CN K_{56} line, and the 1.3 cm continuum emission (see Sollins et al. 2005 for the introduction of the 1.3 cm continuum observation.) Our high resolution observations of the NH_3 (3,3) emissions show complicated morphology with many protrusions in an extended ($\sim 20''$, 0.6 pc) region. The distribution of the dense gas tracer ^{13}CS (5-4) is consistent with a highly non-uniform flattened molecular clump, and may harbor more than one gravitationally bound dense core; the distribution and kinematics of the C^{34}S (5-4) are consistent with ^{13}CS (5-4). The velocity integrated flux of C^{34}S (5-4) is about 1.8 times the velocity integrated flux of the ^{13}CS (5-4). Assuming the abundance ratio of $[^{13}\text{CS}]/[\text{C}^{34}\text{S}]$ is 0.4 (Frerking et al. 1980), the $[\text{CS}]/[\text{C}^{34}\text{S}]$ ratio is 22.6 (Omodaka et al. 1992), the measured C^{34}S (5-4) optical depth ranges from ~ 0.05 to ~ 2 over most of the regions with $>3\sigma$ detections of ^{13}CS (5-4), and the C^{34}S optical depth can be higher than 4 in the densest ($\sim 1''$ scale) regions. These results suggest that the ^{13}CS (5-4) line is at least marginally optically thin in most regions, and therefore is a good tracer of the gas distributions and gas kinematics. In this paper we only show the images of the optically thinner ^{13}CS isotopologues to trace the detailed structures and the kinematics in the inner 0.5 pc clump. The high temperature and high density tracer CH_3CN K_{56} line is only detected in a $3''$ (0.09 pc) region around the UC HII region, which allows us to follow the kinematics of the hot molecular gas directly associated with the UC HII region.

3.3.2. The Position–Velocity Diagram

Before the systematic analysis, we first visually inspect the local structures and the rotational signatures from the position–velocity (PV) diagrams. Figure 5 compares the PV diagram of the NH_3 main hyperfine emission line, the ^{13}CS (5–4) line, and the CH_3CN K_{56} line. The PV cuts are centered at the coordinates of R.A. = $18^{\text{h}}10^{\text{m}}28.64^{\text{s}}$ and decl. = $-19^{\circ}55'49.22''$ with position angle P.A. = 140° . From this figure, we can clearly identify the fast rotational signatures as traced by each molecule; globally, the molecular gas tends to be more redshifted as the angular offset becomes more negative (or less positive). In addition, we found that the motions are consistent with an inward decrease of the specific angular momentum ($\vec{r} \times \vec{v}$). The CH_3CN traces the fast rotating hot toroid, with the rotational velocity gradient of $\sim 100 \text{ kms}^{-1}\text{pc}^{-1}$ at a 0.03 pc radius. In the ^{13}CS (5–4) PV diagram (Figure 5), we observed very prominent rotational signatures from angular offset $-1''$ to $4''$, with an enhanced and lumpy distribution. The velocity gradient of that rotational signature is $\sim 60 \text{ kms}^{-1}\text{pc}^{-1}$ at a 0.08 pc radius. This rotational motion can be gravitationally bound by $430 M_{\odot}$. By comparing the rotation curve traced by ^{13}CS and CH_3CN in the pv diagrams (Figure 5, right), we obviously see a spin-up rotational signature. Note the fast rotating signature traced by the CH_3CN K_{56} line should also contribute in the ^{13}CS PV diagram. However, it is blended with the outer (0.08 pc radius) slower rotating signature. If we use methods such as fitting 2D gaussian to extract the velocity gradient of the hot toroid from the ^{13}CS PV diagram, the confusion of the structure at outer radii leads to an underestimation of the velocity gradient, and also leads to the inconsistency with velocity gradient estimated from the CH_3CN data or other hot core tracer data. The ^{13}CS rotational signature at the 0.08 pc radius is less confused by the kinematics in larger radius since this structure is the dominant feature in that particular angular offset and velocity range.

The line width of the NH_3 (3,3) main hyperfine line is broad (generally $>1 \text{ kms}^{-1}$, and $>>1 \text{ kms}^{-1}$ for low intensity emissions estimated from the moment two map) over the map, but the lines still show the general southeast to northwest velocity gradient of $\sim 15 \text{ kms}^{-1}\text{pc}^{-1}$ at 0.3 pc radius. The observed broad linewidth emissions of ^{13}CS and NH_3 suggest that the molecular core is interacting with outflow or the UC HII regions.

From these PV diagrams, we select the CH_3CN data in the inner 0.05 pc radius, the ^{13}CS (5–4) data in the inner 0.2 pc radius, and the NH_3 (3,3) main hyperfine inversion line in the 0.1–0.3 pc radius to perform the terminal velocity analysis (Section 3.3.3). The selected range of radii ensures each molecule to have greater than 3σ detection.

3.3.3. The Analysis of Terminal Velocity and the Velocity Gradient

The determination of the velocity gradients of the hot core tracers O^{13}CS , OCS , SO_2 , and CH_3CN can be done via Gaussian or other linear fittings. However, the velocity gradients for the ^{13}CS , C^{34}S and NH_3 (3,3) emission structures are less straightforward to estimate. These molecules

are present over a larger region, with rich resolved local density structures and large local velocity dispersions. Any fitting procedure will be biased by the underlying structures in mass, excitation, or velocity.

To sketch the rotation curve in the massive cluster forming regions, we apply the concept of the terminal-velocity method used in extragalactic studies (a review of commonly applied methods for measuring the galaxy rotation curve is given by Sofue and Rubin 2001). Using this method to extract the rotational velocity has the advantage over other fitting procedure since the systematic bias in this method is visually trackable and understandable. From the observed geometry (Section 3.2) of the hot toroid, we assume the system is edge-on. The terminal velocity v_t is then defined by a velocity at which the intensity I equals to

$$I_t = \eta I_{max},$$

and the rotational velocity is defined by

$$v_{rot} = v_t - v_{lsr},$$

where $v_{lsr} = -3 \text{ kms}^{-1}$ for G10.6–0.4, and η is a free parameter ranging between 0 and 1. In G10.6–0.4, the dynamics in the inner and the outer regions are severely blended along the line-of-sight, and the centroid velocity at each radius can be confused by the local dense structures. In such case, the systematic offset of v_{rot} from the real rotation curve is larger than the uncertainties contributed by the thermal or local turbulent motion ($0.5\text{--}1 \text{ kms}^{-1}$ effect).

Before performing the terminal-velocity method, we smooth each image with $1''.3$ kernel to suppress the small-scale fluctuations caused by local intensity peaks. To conservatively demonstrate the decrease of the specific angular momentum with respect to the values in the outer radius reported in the previous low-resolution observations, we purposely choose $\eta = 0.2$, which systematically provide higher estimation of rotational velocity. Instead of explicitly showing the error bar, we present the $\eta = 0.2$ and $\eta = 0.8$ results, of which the comparison gives the sense of uncertainties involved. For the $\eta = 0.8$ case, if at a certain radius the intensity is below ηI_{max} in the entire velocity range, we define v_{rot} at that radius to be the velocity at the peak of the intensity spectrum. We demonstrate the robustness of the analysis from the consistency of rotational velocities traced by different molecules. We define the center of the system at the location where the centroid velocity of the CH_3CN equals to v_{lsr} , and evaluate the velocity gradient at each radius r by v_{rot}/r . The results of the terminal velocity analysis is provided in the next section.

The examples of the ^{13}CS (5-4) terminal-velocities estimated using $\eta = 0.2$ and $\eta = 0.8$ are shown in Figure 6, with the overlay of the pv diagram. From this figure, we see that choosing $\eta = 0.8$ provides significantly lower terminal-velocity. We note that if the molecular gas in an edge-on system rotates concentrically, for a specific line-of-sight, its projected spatial offset is equal to the inner most radius intersecting with that line-of-sight. The motion of the molecular gas at that inner most radius is parallel to the line-of-sight, and the redshift of the emission directly reflects the rotational velocity at that certain radius. In a spin-up system, at a certain spatial offset, the

higher velocity emission is likely to be contributed from the gas in the inner radius. Hence, using $\eta = 0.2$ should better reflect the motions at the inner most radius.

3.3.4. *The Velocity-Gradient and the Specific Angular Momentum*

In Figure 7, we plot the velocity gradients in the axis with position angle of 140° , traced by CH_3CN , ^{13}CS (5-4), and NH_3 (the 2009 C-array data and the D-array data from Ho and Haschick 1986, Keto, Ho, and Haschick 1987), CS (Omodaka et al. 1992) at different radii. The local scattering of the data points reflects the statistical uncertainties in the measurements. According to the measured velocity gradients, we estimate the average specific angular momentum as a function of radius, and summarize the derived results in Figure 8.

From these diagrams, we see that in zones where the rotational velocity can be measured by more than one molecular line, the results from different molecular lines are consistent. This indicates that applying the same η value for different molecular lines is robust. Additionally we see that the estimations with $\eta = 0.2$ and $\eta = 0.8$ are qualitatively consistent with each other. The $\eta = 0.8$ results show lower velocity gradient and lower specific angular momentum. This is because of the bias by the mass along the line-of-sight. The results show that from the 1.5 pc radius to the 0.3 pc radius, the observed specific angular momentum of the molecular gas is nearly conserved, or has a slight decrease. Inside the 0.3 pc ($10''$) radius, the specific angular momentum decreases rapidly, from $\sim 1.5 \text{ pc}\cdot\text{km}\cdot\text{s}^{-1}$ (at 0.3 pc radius) to $< 0.1 \text{ pc}\cdot\text{km}\cdot\text{s}^{-1}$ (at 0.03 pc radius). From the results, we find a turnover radius r_T of about 0.3 pc within which specific angular momentum experiences a significant loss. For $r < r_T$, we find a specific angular momentum loss rate of $\sim 5.2 \text{ pc}\cdot\text{km}\cdot\text{s}^{-1}$ per parsec.

We note that the diagnostic model in Keto (1990) suggested that the gas flow does not conserve angular momentum on any scale. However, that previous model was constructed based on the observations of the NH_3 line emissions with $\sim 10''$ (0.3 pc) resolution, and the observations of the NH_3 line absorption with $\sim 0''.3$ (0.009 pc) resolution. Inward of the 0.3 pc radius, the model had been uncertain owing to insufficient sampling of the spatial scales. Our new observations presented in this paper can be viewed as a more detailed demonstration of the decreasing specific angular momentum suggested in the previous model.

In addition to the terminal-velocity method, we also make alternative estimations of the velocity gradient by referencing to intensity-weighted mean velocities. We perform the linear regression fittings to obtain the slopes of the intensity-weighted mean velocity, which can be interpreted as velocity gradients. The results are summarized in Table 3. When fitting the ^{13}CS velocity, we exclude the emission enclosed by the dashed box in Figure 5 since the velocity of the brightest component in that region is close to the systemic velocity of the entire molecular cloud ($-3 \text{ km}\cdot\text{s}^{-1}$), will be dominated by that motion. The extended emission in that region may be the corresponding outflow. The results are shown in Table 3. For the CH_3CN line, since the scale of the synthesized

beam is comparable to the scale of the emission region, we perform linear regression fittings of the gradients of intensity-weighted mean angular offset along the velocity axis. The emission at angular offset $\sim 0''$ with velocity $> 2 \text{ kms}^{-1}$ does not have a high signal-to-noise ratio. Thus it is not clear whether it is a real structure. We therefore provide two fitting results; the lower velocity gradient value is obtained by excluding the data with velocity $> 2 \text{ kms}^{-1}$.

The observed velocity gradients of the OCS (19-18) line, the O^{13}CS (19-18) line, the SO_2 18(1,17)-18(0,18) and 5(2,4)-4(1,3) lines, and the CH_3CN lines are consistent. The errors take into account the uncertainties introduced by the local velocity dispersions at both ends of the rotational signatures. These values are also consistent with the velocity gradient of the CH_3CN line obtained from the terminal-velocity method (Figure 7). Assuming that the hot and dense core is edge on, the observed velocity gradients can be gravitationally bound by $\sim 200 \text{ M}_\odot$. However, from the Lyman continuum emission rate, Sollins et al. (2005) estimated the stellar mass embedded in the UC HII region to be $\sim 175 \text{ M}_\odot$, which dominates the enclosed mass estimated from the rotation curves. We therefore suggest that the geometry of the hot and dense molecular gas in the central $3''$ (0.09 pc) region is a rotating ring/torus which encircles the UC HII region. The velocity gradient of the NH_3 line obtained from the linear regression fitting is significantly lower than those values obtained from the terminal-velocity method with $\eta=0.2$, however, consistently suggests the low specific angular momentum inward of the 0.3 pc radius.

The comparison of the CH_3CN distribution with the ^{13}CS distribution (Figure 4) suggests that the rotational centers of the hot toroid and the lumpy ^{13}CS ring/toroid are offset by a few arcseconds. The peak velocities of CH_3CN and ^{13}CS are also offset by a few kms^{-1} from the overall systemic velocity of -3 kms^{-1} . These offsets can be explained by fragmentation within the central core, resulting in peculiar motions, as well as opacity/excitation and chemical effects which may bias the peak emission velocities. Moreover, the motions within the central 0.3 pc core appear quite turbulent with velocity dispersions $> 5 \text{ kms}^{-1}$. At smaller scales ($< 0.1 \text{ pc}$ radius), strong magnetic braking by a few mG magnetic field may efficiently remove the specific angular momentum (see Keto, Ho & Haschick 1987, and Girart et al. 2009 for derivations). Between 0.1 and 0.3 pc scale, it is likely that a large fraction of the specific angular momentum remains in the orbital motions. This results in reduced specific angular momentum at the scale of the fragments which are able to form and which are detected. Note that the resolved NH_3 protrusions and the large velocity dispersion of the ^{13}CS (5-4) also suggest that the outflow, shock, and the induced turbulence may be closely related to the transfer of angular momentum. The relative importance of these processes, and other possible ones, remains to be elucidated by future observations.

3.4. Mass Estimates Using Molecular Lines

3.4.1. The Hot Toroid

We estimate the observed molecular mass of the hot toroid from the integrated intensities of the CH_3CN $J=12-11$, $K=5, 6$, and the OCS , O^{13}CS $J=19-18$ emissions. We suggest that the hot molecular gas with an average temperature of $T \sim 300$ K (see also Klaassen et al. 2009: 323 ± 105 K) dominates the contribution to the flux in these transitions. By adopting the CH_3CN abundance $[\text{CH}_3\text{CN}]/[\text{H}_2] = 10^{-8} - 10^{-7}$ (Kalenskii et al. 2000; Klaassen et al. 2009), and assuming CH_3CN $J=12$, $K=5, 6$ transitions are optically thin, which is typically true in hot molecular cores, the derived H_2 mass from $K=5$ lines in the central 0.06 pc region is $12-1.2 M_\odot$, and the derived H_2 mass from $K=6$ lines in the central 0.06 pc region is $7.2-0.72 M_\odot$. The deviation of the derived H_2 mass from the two transitions may be caused by the error in our temperature assumption.

Assuming that the O^{13}CS $J=19-18$ is generally optically thin, we estimate the lower limit for the H_2 mass as traced by O^{13}CS to be $15-15000 M_\odot$ for the range of the abundance ratio $[\text{OCS}]/[\text{H}_2]$ of $10^{-6} - 10^{-9}$ (see Viti et al. 2004 and references therein for the abundance ratio). Since the hot toroid is interacting with the central OB cluster, the ionized gas, and the outflows, we expect a highly enhanced OCS abundance in the detected region, and the molecular mass of the hot toroid should be closer to the lower estimate of $15 M_\odot$.

By observing the NH_3 (3,3) inversion transition, Keto, Ho, and Haschick (1988) estimated the H_2 mass in the similar region to be $3-60 M_\odot$ using the assumption of abundance $[\text{NH}_3]/[\text{H}_2] = 10^{-6} - 10^{-7}$ (Ho and Townes 1983). Considering the uncertainties in the CN_3CN , OCS and NH_3 abundance and the foreground contribution to the NH_3 (3,3) line, the mass estimates by these three molecules are consistent. By comparing the binding mass of the ^{13}CS motion (at 0.08 pc radius: $300 M_\odot$) with the mass of the OB cluster ($175 M_\odot$) and the mass of the hot toroid traced by the CH_3CN line, we argue that the bulk of the ^{13}CS dense lumpy ring/toroid is encircling the hot toroid and the OB cluster. The observed velocities are consistent with gravitationally bound motions due to the enclosed mass at each radius.

3.4.2. The Larger Scale Mass

Assuming that the abundance ratio $[\text{CS}]/[\text{H}_2]$ is $10^{-6} - 10^{-9}$ (Viti et al. 2004), an average temperature of 50 K, and assuming optically thin emission, we estimate the lower limit of the H_2 mass traced by the ^{13}CS (5-4) to be $10^2 - 10^5 M_\odot$. By adopting the abundance ratio $[\text{CS}]/[\text{H}_2] = 10^{-9}$, Omodaka et al. (1992) estimate the H_2 mass of the entire clump traced by $\text{C}^{34}\text{S}/\text{CS}$ (2-1) to be $4 \cdot 10^4 M_\odot$, which agrees well with our estimate. Using C^{18}O (2-1), Ho, Terebey and Turner (1994) estimated the H_2 mass in the central $30''$ (0.9 pc) region to be $2500 M_\odot$, suggesting that the average

value of $[\text{CS}]/[\text{H}_2]^5$ is close to 10^{-7} – 10^{-8} . We note that from this large scale ($\sim 1\text{pc}$) core, about 10% of the mass has condensed and formed the visible massive stars, and only 10% of the stellar mass is in a remnant hot toroid. The star formation efficiency is very high.

3.4.3. The Centrifugal Velocities

In Figure 7, we summarize the required velocity gradients to balance against the gravity of the enclosed molecular and stellar masses at a number of radii. Values of NH_3 mass, CS mass, C^{18}O mass, and the embedded stellar mass are quoted from the literature (Keto, Ho and Haschick 1987; Omodaka et al. 1992; Ho, Terebey and Turner 1994; Sollins et al. 2005). By comparing the required velocity gradients with the measured velocity gradients, we suggest that there may be a crossover at about 0.3 pc radius. The dynamics of the gas in the entire region is dominated by gravity. Inward of the crossover, some mechanism removes excess angular momentum allowing the flow to maintain a high inward velocity and high accretion rate even as the flow progresses to smaller and smaller radii. Note that the location of this crossover is consistent with the turnover radius of the specific angular momentum (Figure 8). The formation of a flattened structure with spin-up motions within a fluffy core, as seen in Figure 4, is consistent with this scenario.

4. Conclusions

We have carried out arcsecond resolution SMA and VLA/eVLA observations in the massive cluster forming region G10.6–0.4. The main results are as follows:

- By comparing the $\text{O}^{13}\text{CS}/\text{OCS}$ ratio with the NH_3 (3,3) main and satellite hyperfine line ratio, we confirmed a $\sim 2'' \times 1''$ rotationally flattened dense toroid around the UC HII region. Owing to the uncertainties in abundance, the molecular mass of the dense toroid can be from a few to a few tens of solar mass. The dense toroid is marginally rotationally supported against the gravity of the encircled stellar cluster of $\sim 175 M_\odot$.
- Using the terminal-velocity method, we follow the rotational velocity from the 0.3 pc scale radius to the 0.03 pc scale radius. The results suggest a rapid decrease of specific angular momentum inward of the 0.3 pc radius, with a mean specific angular momentum loss rate of $\sim 5.2 \text{ pc} \cdot \text{kms}^{-1}$ per parsec.
- We detect local structures in the ^{13}CS (5-4) observations, suggesting that the system is clumpy and self-gravitating. The fragmentation may account for 25%–40% of the loss of specific angular momentum.

⁵The $[\text{CS}]/[\text{H}_2]$ ratio in Orion hot core, compact ridge, and extended ridge is about 10^{-8} (Sutton et al. 1995; Charnley 1997).

Baobab Liu thanks Meri Stanley and Mark Claussen for help in preparing the VLA/eVLA observations. *Facilities:* SMA, VLA

REFERENCES

- Araya, E., Hofner, P., Kurtz, S., Bronfman, L., & DeDeo, S. 2005, *ApJS*, 157, 279
- Beltrán, M. T., Cesaroni, R., Neri, R., Codella, C., Furuya, R. S., Testi, L., & Olmi, L. 2004, *ApJ*, 601, L187
- Beltrán, M. T., Cesaroni, R., Neri, R., Codella, C., Furuya, R. S., Testi, L., & Olmi, L. 2005, *A&A*, 435, 901
- Beuther, H., Schilke, P., Sridharan, T. K., Menten, K.-M., Walmsley, C. M., & Wyrowski, F. 2002, *A&A*, 383, 892
- Beuther, H., & Walsh, A. J. 2008, *ApJ*, 673, L55
- Caselli, P., Hasegawa, T. I., & Herbst, E. 1993, *ApJ*, 408, 548
- Casoli, F., Combes, F., Dupraz, C., Gerin, M., & Boulanger, F. 1986, *A&A*, 169, 281
- Caswell, J. L., Murray, J. D., Roger, R. S., Cole, D. J., & Cooke, D. J. 1975, *A&A*, 45, 239
- Cesaroni, R., Walmsley, C. M., Koempe, C., & Churchwell, E. 1991, *A&A*, 252, 278
- Cesaroni, R., Galli, D., Lodato, G., Walmsley, C. M., & Zhang, Q. 2007, *Protostars and Planets V*, 197
- Charnley, S. B. 1997, *ApJ*, 481, 396
- Corbel, S., & Eikenberry, S. S. 2004, *A&A*, 419, 191
- Churchwell, E., Walmsley, C. M., Wood, D. O. S., & Steppe, H. 1990, *IAU Colloq. 125: Radio Recombination Lines: 25 Years of Investigation*, 163, 83
- Churchwell, E., Walmsley, C. M., & Wood, D. O. S. 1992, *A&A*, 253, 541
- Downes, D., Wilson, T. L., Bieging, J., & Wink, J. 1980, *A&AS*, 40, 379
- Fish, V. L., Reid, M. J., Argon, A. L., & Zheng, X.-W. 2005, *ApJS*, 160, 220
- Frerking, M. A., Wilson, R. W., Linke, R. A., & Wannier, P. G. 1980, *ApJ*, 240, 65
- Furuya, R. S., Cesaroni, R., Takahashi, S., Codella, C., Momose, M., & Beltrán, M. T. 2008, *ApJ*, 673, 363

- Galván-Madrid, R., Keto, E., Zhang, Q., Kurtz, S., Rodríguez, L. F., & Ho, P. T. P. 2009, *ApJ*, 706, 1036
- Gibb, E., Nummelin, A., Irvine, W. M., Whittet, D. C. B., & Bergman, P. 2000, *ApJ*, 545, 309
- Girart, J. M., Beltrán, M. T., Zhang, Q., Rao, R., & Estalella, R. 2009, *Science*, 324, 1408
- Guilloteau, S., Forveille, T., Baudry, A., Despois, D., & Goss, W. M. 1988, *A&A*, 202, 189
- Ho, P. T. P., & Haschick, A. D. 1981, *ApJ*, 248, 622
- Ho, P. T. P., Vogel, S. N., Wright, M. C. H., & Haschick, A. D. 1983, *ApJ*, 265, 295
- Ho, P. T. P., & Townes, C. H. 1983, *ARA&A*, 21, 239
- Ho, P. T. P., & Haschick, A. D. 1986, *ApJ*, 304, 501
- Ho, P. T. P., Klein, R. I., & Haschick, A. D. 1986, *ApJ*, 305, 714
- Ho, P. T. P., Moran, J. M., & Lo, K. Y. 2004, *ApJ*, 616, L1
- Ho, P. T. P., Terebey, S., & Turner, J. L. 1994, *ApJ*, 423, 320
- Hofner, P., & Churchwell, E. 1996, *A&AS*, 120, 283
- Hofner, P., Wyrowski, F., Walmsley, C. M., & Churchwell, E. 2000, *ApJ*, 536, 393
- Kalenskii, S. V., Promislov, V. G., Alakoz, A., Winnberg, A. V., & Johansson, L. E. B. 2000, *A&A*, 354, 1036
- Keto, E. R., Ho, P. T. P., & Haschick, A. D. 1987, *ApJ*, 318, 712
- Keto, E. R., Ho, P. T. P., & Haschick, A. D. 1988, *ApJ*, 324, 920
- Keto, E. R. 1990, *ApJ*, 355, 190
- Keto, E. 2002, *ApJ*, 586, 754
- Keto, E., & Wood, K. 2006, *ApJ*, 637, 850
- Keto, E., Zhang, Q., & Kurtz, S. 2008, *ApJ*, 672, 423
- Klaassen, P. D., Wilson, C. D., Keto, E. R., & Zhang, Q. 2009, *ApJ*, 703, 1308
- Lis, D. C., Serabyn, E., Keene, J., Dowell, C. D., Benford, D. J., Phillips, T. G., Hunter, T. R., & Wang, N. 1998, *ApJ*, 509, 299
- Müller, H. S. P., Thorwirth, S., Roth, D. A., & Winnewisser, G. 2001, *A&A*, 370, L49

- Müller, H. S. P., Schlöder, F., Stutzki, J., & Winnewisser, G. 2005, *Journal of Molecular Structure*, 742, 215
- Omodaka, T., Kobayashi, H., Kitamura, Y., Nakano, M., & Ishiguro, M. 1992, *PASJ*, 44, 447
- Sofue, Y., & Rubin, V. 2001, *ARA&A*, 39, 137
- Sollins, P. K., Zhang, Q., Keto, E., & Ho, P. T. P. 2005, *ApJ*, 624, L49
- Sollins, P. K., Zhang, Q., Keto, E., & Ho, P. T. P. 2005, *ApJ*, 631, 399
- Sollins, P. K., & Ho, P. T. P. 2005, *ApJ*, 630, 987
- Sutton, E. C., Peng, R., Danchi, W. C., Jaminet, P. A., Sandell, G., & Russell, A. P. G. 1995, *ApJS*, 97, 455
- Viti, S., Collings, M. P., Dever, J. W., McCoustra, M. R. S., & Williams, D. A. 2004, *MNRAS*, 354, 1141
- Walmsley, C. M., & Ungerechts, H. 1983, *A&A*, 122, 164
- Wood, D. O. S., & Churchwell, E. 1989, *ApJ*, 340, 265
- Wu, J., & Evans, N. J., II 2003, *ApJ*, 592, L79
- Zhang, Q., Hunter, T. R., Brand, J., Sridharan, T. K., Molinari, S., Kramer, M. A., & Cesaroni, R. 2001, *ApJ*, 552, L167
- Zhang, Q., Hunter, T. R., Brand, J., Sridharan, T. K., Cesaroni, R., Molinari, S., Wang, J., & Kramer, M. 2005, *ApJ*, 625, 864

Transition	Frequency (GHz)	E_u (K)	Eins. A. (s^{-1})	Note
SO ₂ 5(2,4)–4(1,3)	241.615779	23.5	$8.46 \cdot 10^{-5}$	
SO ₂ 18(1,17)–18(0,18)	240.942788	162.0	$7.02 \cdot 10^{-5}$	
OCS 19–18	231.060991	110.2	$3.58 \cdot 10^{-5}$	
O ¹³ CS 19–18	230.317500	109.9	$3.54 \cdot 10^{-5}$	
NH ₃ (3,3)	23.870129	124.5	$2.56 \cdot 10^{-7}$	
¹³ CS (5–4)	231.220768	33.1	$2.51 \cdot 10^{-4}$	
CH ₃ CN 12(5)–11(5)	220.641096	242	$7.6 \cdot 10^{-4}$	K ₅₆ line
CH ₃ CN 12(6)–11(6)	220.594438	319	$6.9 \cdot 10^{-4}$	

Table 1: Table of the selected molecular transitions. The quantum number of the transitions are listed in the first column. Their frequencies and upper-level-energy are listed in the second and the third column. The Einstein coefficient of each transition is listed in the fourth column. The last two transitions are averaged to be the K₅₆ line.

Transition	bpa	b_{maj}	b_{min}	uv Sampling Range (k λ)	rms in Image (JY/beam)
SO ₂ 5(2,4)–4(1,3)	21 $^\circ$	0 $''$.62	0 $''$.43	6–393	0.08
SO ₂ 18(1,17)–18(0,18)	23 $^\circ$	0 $''$.62	0 $''$.43	6–393	0.08
OCS 19–18	22 $^\circ$	0 $''$.62	0 $''$.43	6–393	0.08
O ¹³ CS 19–18	73 $^\circ$	0 $''$.97	0 $''$.61	6–393	0.05
NH ₃ (3,3)	0.96 $^\circ$	1 $''$.8	1 $''$.2	2.2–270	0.008
¹³ CS (5–4)	80 $^\circ$	1 $''$.3	0 $''$.66	5.4–393	0.05
CH ₃ CN 12(5)–11(5)	56 $^\circ$	1 $''$.5	1 $''$.1	26–145	0.12
CH ₃ CN 12(6)–11(6)					

Table 2: The observational parameters.

Transition	Fitted Velocity Gradient (kms ^{−1} pc ^{−1})	Radius (pc)
CH ₃ CN K ₅₆	$146.0^{+27}_{-20}/109.9^{+18}_{-13}$	0.027
SO ₂ 5(2,4)–4(1,3)	95^{+40}_{-10}	
SO ₂ 18(1,17)–18(0,18)	105^{+60}_{-25}	
OCS 19–18	85^{+40}_{-20}	
O ¹³ CS 19–18	85^{+40}_{-20}	
¹³ CS (5–4)	38.2 ± 2.8	0.075
¹³ CS (5–4)	15.6 ± 1.5	0.15
NH ₃ (3,3)	8.7 ± 2.2	0.27

Table 3: The fitted velocity gradients. The velocity gradients of the hot core type tracers are evaluated in the same spatial region. See Section 3.3.4 for the details of fittings.

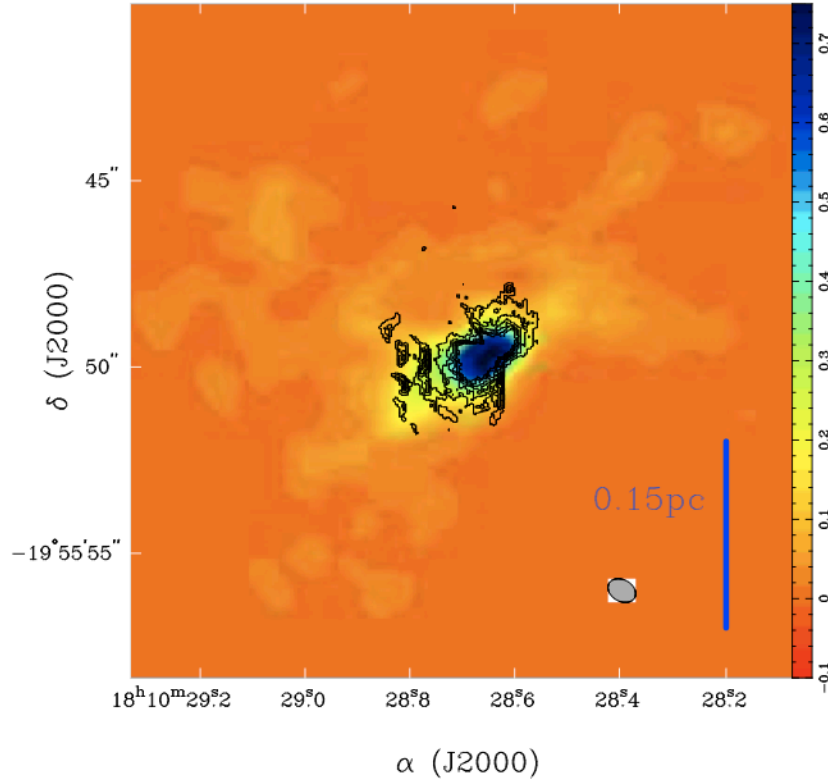


Figure 1: 1.3 mm continuum image (color) and the 13 mm continuum image (contour). The synthesized beam of the 1.3 mm continuum image is shown in bottom right of this figure. Labels of the color bar have the unit of Jy beam^{-1} . Contours start from 5% of the 13 mm continuum peak, with 5% steps.

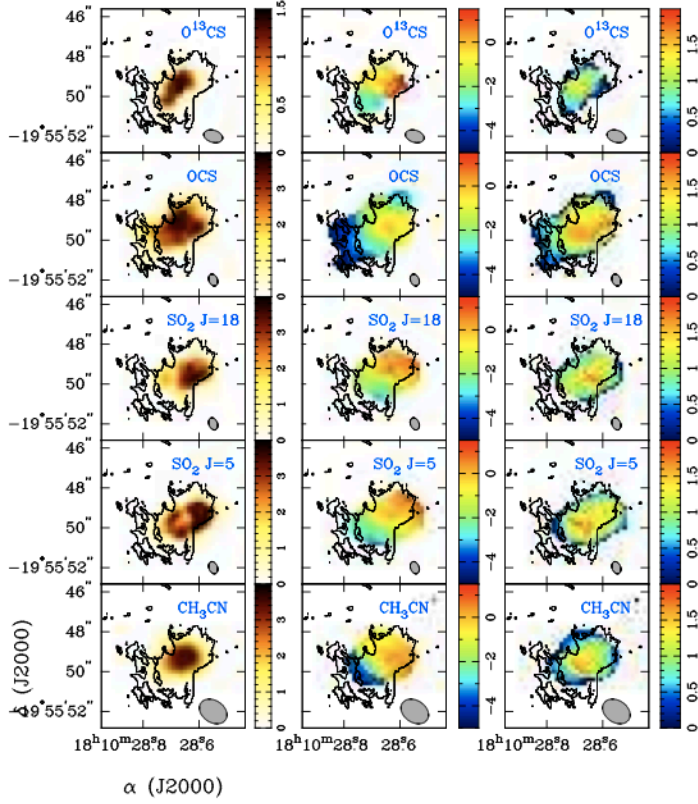


Figure 2: **Left:** Moment zero maps of the O^{13}CS (19–18) line, the OCS (19–18) line, and the SO_2 18(1,17)–18(0,18) and 5(2,4)–4(1,3) lines, and the CH_3CN K_{56} line. Contours show the 3% level of the 1.3 cm continuum emission. The unit of the color bar is $(\text{Jy beam}^{-1}) \cdot (\text{m/s})$. **Middle:** Moment one maps of the O^{13}CS (19–18) line, the OCS (19–18) line, and the SO_2 18(1,17)–18(0,18) and 5(2,4)–4(1,3) lines, and the CH_3CN K_{56} line. Contours show the 3% level of the 1.3 cm continuum emission. The unit of the color bar is km s^{-1} . **Right:** Moment two maps of the O^{13}CS (19–18) line, the OCS (19–18) line, and the SO_2 18(1,17)–18(0,18) and 5(2,4)–4(1,3) lines, and the CH_3CN K_{56} line. Contours show the 3% level of the 1.3 cm continuum emission. The unit of the color bar is km s^{-1} .

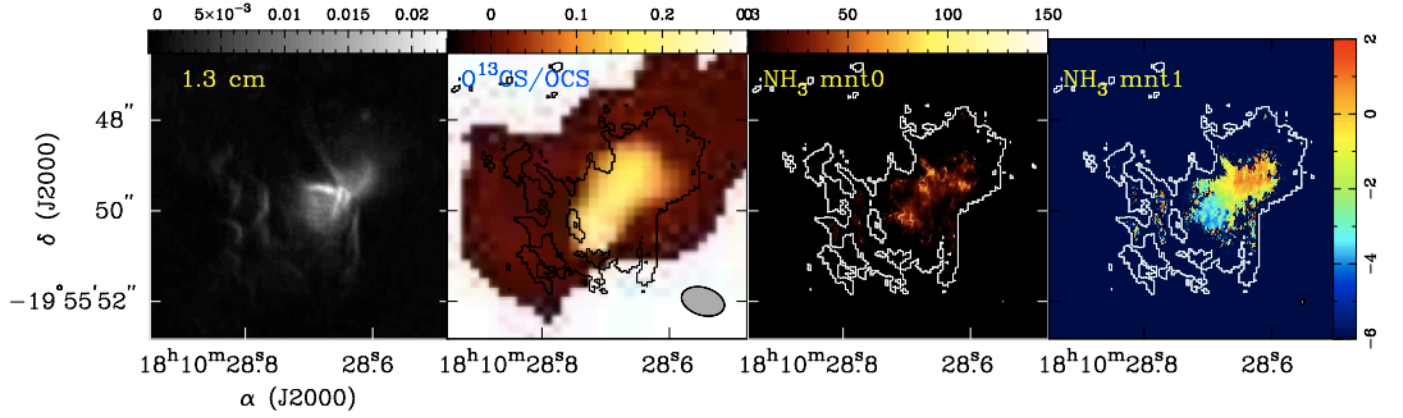


Figure 3: **Left:** VLA A-array 1.3 cm continuum map (Jy/beam). **Middle Left:** Ratio of the O^{13}CS and OCS velocity integrated intensity. **Middle Right:** Velocity integrated NH_3 (3,3) satellite line optical depth ($\tau \cdot \text{kms}^{-1}$). **Right:** Optical depth weighted averaged velocity of the NH_3 (3,3) satellite line (kms^{-1}). Contours show the 3% level of the 1.3 cm continuum emission. The VLA A-array 1.3 cm continuum and the NH_3 (3,3) satellite line data are reprocessed. See Sollins et al. (2005) and Sollins and Ho (2005) for the detailed configurations of these VLA observations.

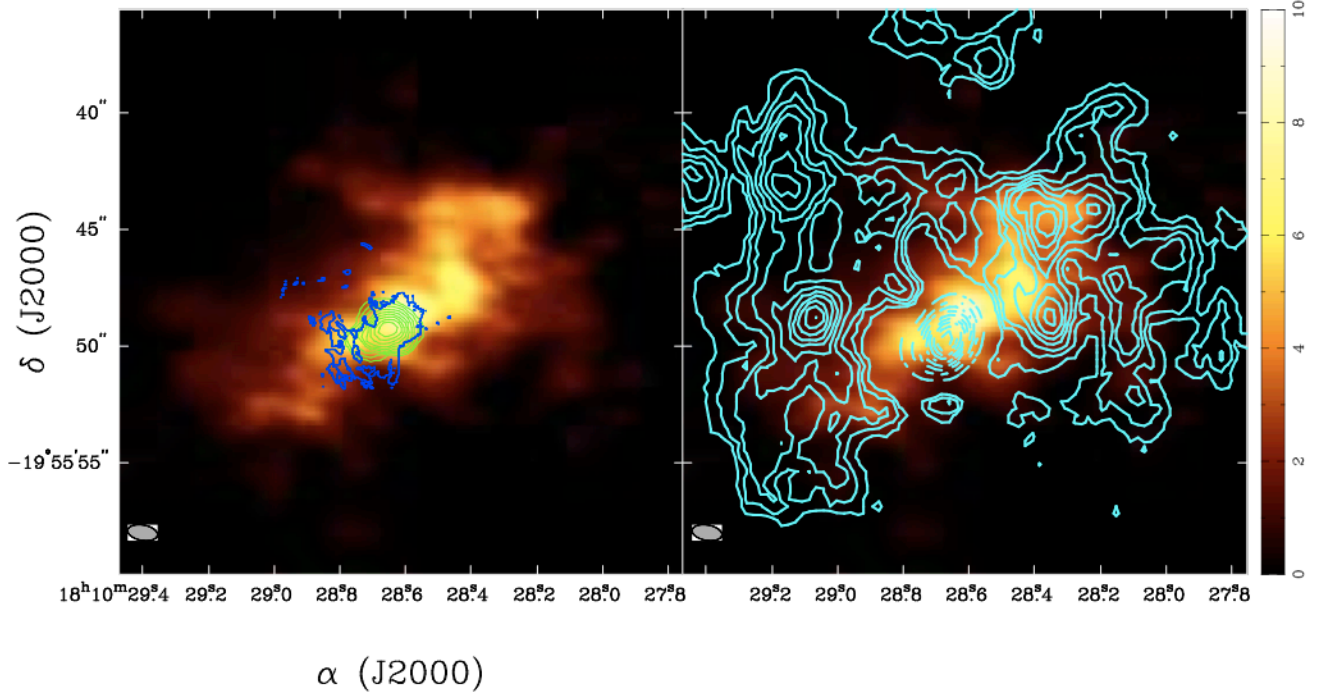


Figure 4: **Left:** Moment zero map of the ^{13}CS J=5-4 line (color scale), the CH_3CN J=12, K=5, 6 lines (green), and the 1.3 cm continuum image (blue). **Right:** Moment zero map of the NH_3 (3,3) main hyperfine emission line (cyan) and the ^{13}CS J=5-4 line (color scale). The positive contours of the moment zero maps start from 10% of their emission peak value, with 10% steps (solid); the negative contours of the moment zero maps start from -200% of their emission peak value, with -200% steps (dashed). The 1.3 cm continuum is only shown in 3% peak value contour. The synthesized beam of the ^{13}CS (5-4) map is shown at the bottom left of the image. The unit of the color bar is $(\text{Jy beam}^{-1}) \cdot (\text{km s}^{-1})$.

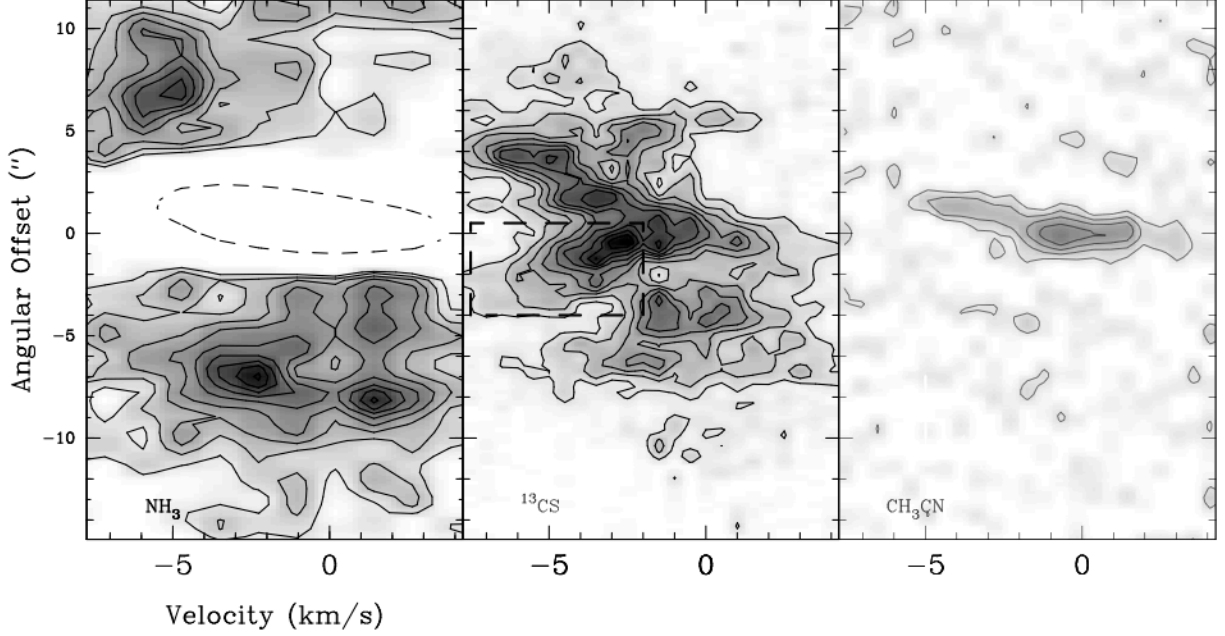


Figure 5: **Left:** The PV diagram of the NH₃ (3,3) main hyperfine line. Solid contours start from 10% of the emission peak, with 10% intervals. The dashed contour shows the level of -500% emission peak. Black line shows the velocity gradient of $14 \text{ km s}^{-1} \text{ pc}^{-1}$. **Middle:** The PV diagram of the ¹³CS (5-4) line. Contours start from 10% of the emission peak, with 10% intervals. Black lines show the velocity gradient of 12 and $53 \text{ km s}^{-1} \text{ pc}^{-1}$. The region enclosed by a dashed box in this panel is excluded while performing linear fittings of the velocity gradients. **Right:** The PV diagram of the CH₃CN line. Contours start from 20% of the emission peak, with 20% intervals. Black lines show the velocity gradient of 100 and $133 \text{ km s}^{-1} \text{ pc}^{-1}$. All PV cuts are centered at the coordinates of R.A. = $18^h 10^m 28^s.64$ and decl. = $-19^\circ 55' 49''.22$ with position angle P.A. = 140° .

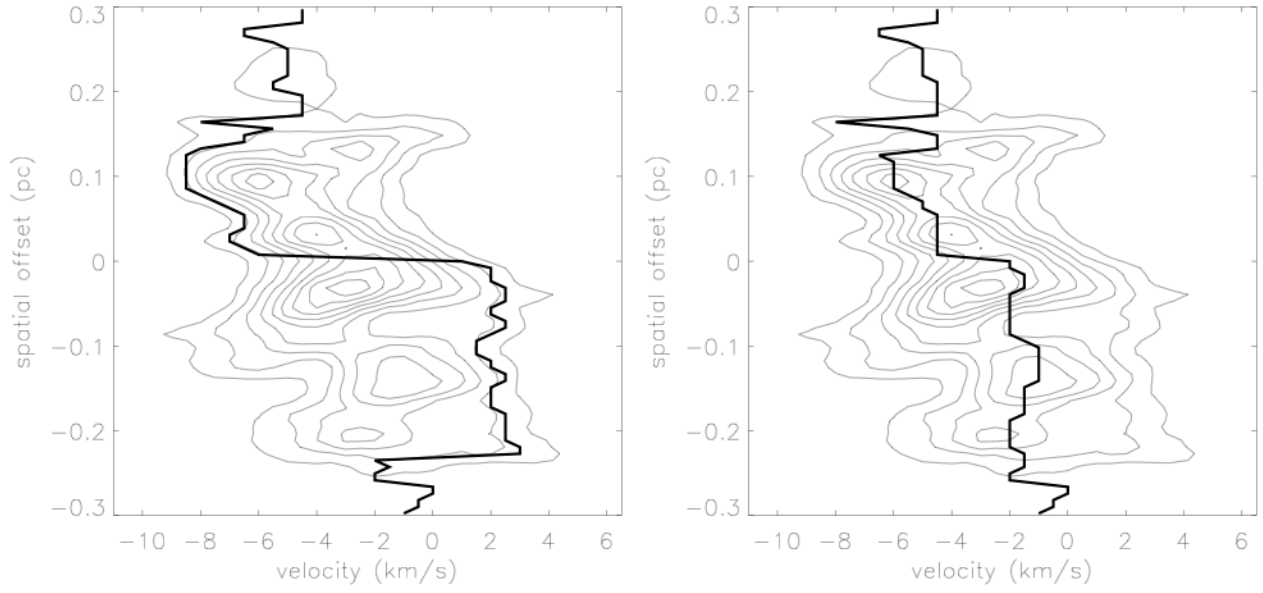


Figure 6: Examples of the results terminal velocity tracing method on ^{13}CS (5-4) PV diagram. The terminal velocities defined by $\eta = 0.2$ (left) and $\eta = 0.8$ (right) are presented in black lines.

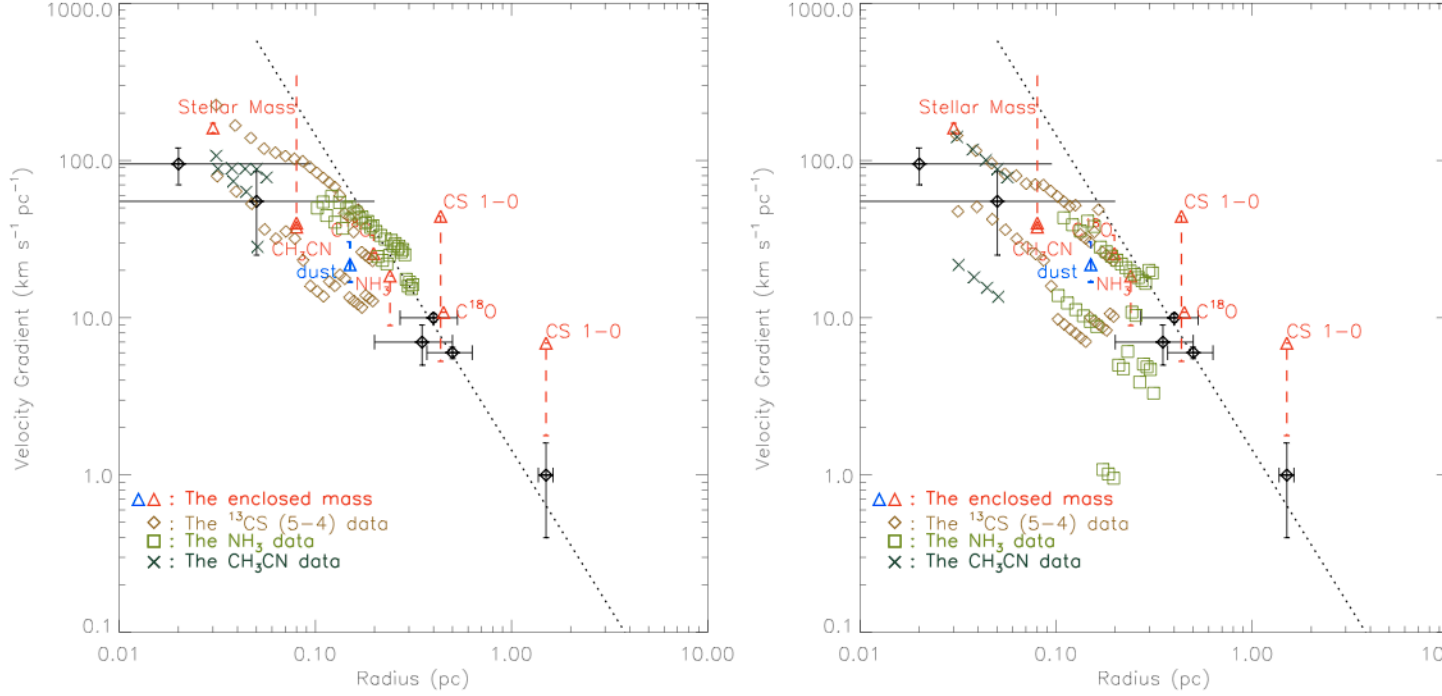


Figure 7: Velocity gradient at different radii. The dark green crosses represent the CH₃CN data; the orange diamonds represent the ¹³CS (5–4) data; and the green squares represent the NH₃ (3,3) main hyperfine inversion line data. The values in the left panel and the right panel are estimated using $\eta = 0.2$ and $\eta = 0.8$, respectively. **Black:** Velocity gradients at different radii reported by previous observations (From left to right: NH₃ (3,3) main hyperfine line (Keto, Ho & Haschick 1988); NH₃ (3,3) main hyperfine line (Keto, Ho & Haschick 1987); NH₃ (3,3) main hyperfine line (Keto, Ho & Haschick 1987); NH₃ (1,1) main hyperfine line (Ho & Haschick 1986); CS (1-0) (Omodaka et al. 1992); NH₃ (1,1) main hyperfine line (Keto, Ho & Haschick 1987)). **Red:** The necessary velocity gradients to balance the enclosed stellar and molecular mass estimated by the labeled molecules. Dashed error-bars take into account the uncertainties caused by abundance variations. We quote the estimated embedded stellar mass of 175 M_⊙ from Sollins et al. (2005). At the 1.5 pc radius, we provide the limit of the velocity gradient assuming that the embedded mass is 2500–40000 M_⊙. **Blue:** The necessary velocity gradients to balance the embedded stellar and molecular mass estimated by the 1.3 mm continuum. The dotted line sketches the expected velocity gradient assuming that the measured specific angular momentum at the radius of 0.5 pc is conserved.

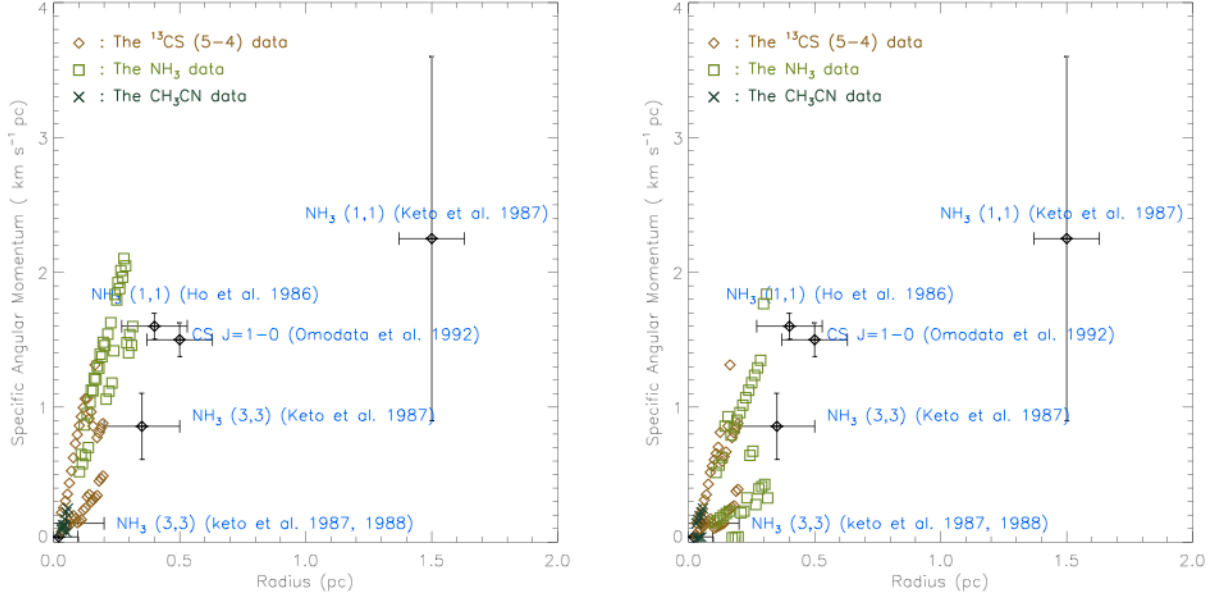


Figure 8: Specific angular momentum at different radii traced by the available molecular line data. The dark green cross represent the CH₃CN data; the orange diamonds represents the ¹³CS (5-4) data; and the green squares represent the NH₃ (3,3) main hyperfine inversion line data. The values in the left panel and the right panel are estimated using $\eta = 0.2$ and $\eta = 0.8$, respectively. Black circles show the values reported by previous observations.